

Influence of planform geometry and momentum ratio on thermal mixing at a stream confluence with a concordant bed

George Constantinescu¹ · Shinjiro Miyawaki² ·
Bruce Rhoads³ · Alexander Sukhodolov⁴

Received: 28 September 2015 / Accepted: 28 April 2016 / Published online: 5 May 2016
© Springer Science+Business Media Dordrecht 2016

Abstract The effects of planform geometry and momentum flux ratio on thermal mixing at a stream confluence with concordant bed morphology are investigated based on numerical simulations that can capture the dynamics of large-scale turbulence. In two simulations, the bathymetry and asymmetrical planform geometry are obtained from field experiments and the momentum flux ratio is set at values of one and four. These two conditions provide the basis for studying differences in thermal mixing processes at this confluence when the wake mode and the Kelvin–Helmholtz mode dominate the development of coherent structures within the mixing interface (MI). The effects of channel curvature and angle between the two incoming streams on thermal mixing processes are investigated based on simulations conducted with modified planform geometries. Two additional simulations are conducted for the case where the upstream channels are parallel but not aligned with the downstream channel and for the zero-curvature case where the upstream channels are parallel and aligned with the downstream channel. The simulations highlight the influence of large-scale coherent structures within the MI and of streamwise-oriented vortical (SOV) cells on thermal mixing processes within the confluence hydrodynamics zone. Simulation results demonstrate the critical role played by the SOV cells in promoting large-scale thermal mixing for cases when such cells form in the immediate vicinity of the MI and in modifying the shape of the thermal MI within cross sections of the downstream channel—predictions consistent with empirical measurements of thermal mixing at the confluence. The set of numerical simulations reveal that the degree of

✉ George Constantinescu
sconstan@engineering.uiowa.edu

¹ Department of Civil and Environmental Engineering and IIHR-Hydroscience and Engineering, The University of Iowa, Iowa City, IA 52242, USA

² IIHR-Hydroscience and Engineering, The University of Iowa, Iowa City, IA 52242, USA

³ Department of Geography and Geographic Information Science, University of Illinois at Urbana-Champaign, Urbana, IL 61801, USA

⁴ Department of Ecohydrology, Institute of Freshwater Ecology and Inland Fisheries, Müggelseedamm 310, 12587 Berlin, Germany

thermal mixing occurring within the confluence hydrodynamic zone varies dramatically with planform geometry and incoming flow conditions. In some cases thermal mixing at the downstream end of the confluence hydrodynamic zone is limited to the MI and its immediate vicinity, whereas in others substantial thermal mixing has occurred over most of the cross-sectional area of the flow. Overall, the simulations highlight the flow conditions and the controls of these conditions that influence mixing within the immediate vicinity of a confluence.

Keywords River confluences · Vortices · Mixing layers · Turbulent mixing

1 Introduction

River confluences are fundamental elements of natural drainage networks that play a critical role in regulating the movement of water and sediment through river systems [24, 43, 64]. In many cases, the incoming flows at confluences are characterized by unequal temperatures, suspended sediment concentrations, salinities, organic matter content and nutrient loads [27, 32, 54, 63]. Spatial heterogeneity of these properties and constituents downstream of confluences is an important factor influencing water quality and ecosystem processes in river networks [49]. The spatial extent of the region downstream of the confluence characterized by significant spatial heterogeneity of the water properties depends on the dynamics of mixing and, in particular, on how fast mixing between the two streams takes place. Being able to quantitatively characterize mixing at river confluences is also critical for cases when a pollutant is advected into a larger channel by a tributary flow. The dispersion of the pollutant within the main channel and the rate of decay of the pollutant concentration downstream of the confluence are directly related to lateral mixing rates, i.e. how fast mixing occurs between the main-channel and tributary flows.

Confluences are among the most complex hydrodynamic environments in river systems. The region affected by the interaction of flows from separate streams, where three-dimensionality of flow structure is greatly enhanced, is referred to as the confluence hydrodynamic zone [52]. This zone generally extends several channel widths downstream of the junction corner. At the confluence apex, mixing is initiated along the mixing interface (MI) that develops between the two confluent streams with different properties (e.g., mean velocity, temperature, salinity, suspended sediment load). Two of the main characteristics of the flow within the confluence hydrodynamic zone are that the flow conditions are relatively shallow (bed friction affects the development of the MI) and that large-scale turbulent coherent structures form inside and in the vicinity of the MI. The unsteady dynamics of these coherent structures play an important role in determining how fast the two streams mix [12].

The position of the MI and the structure of the flow in its vicinity depend on the momentum ratio between the two incoming streams ($Mr = (\rho_2 Q_2 U_{20}) / (\rho_1 Q_1 U_{10})$, where ρ_i , Q_i and U_{i0} are density, discharge and bulk velocity in the lateral [$i = 2$] and main [$i = 1$] tributaries), the angular orientation of the two tributary channels with respect to alignment of the downstream channel (the angles between the centerlines of the main and lateral tributaries are denoted α_1 and α_2 , respectively), and the degree of bed discordance [16]. The growth of the large-scale quasi-2D MI eddies downstream of the formation region enhances transverse turbulent diffusion and thus mixing between the two streams.

Constantinescu et al. [18] proposed a classification of MI dynamics that distinguishes between two main types of MIs. In the Kelvin–Helmholtz (KH) mode, the horizontal velocity difference between the two sides of the MI is significant. The MI contains predominantly co-rotating large-scale quasi two-dimensional (2D) eddies whose growth is driven by the KH instability [62] and vortex pairing, similar to a shallow mixing layer developing between two parallel streams [3, 12]. In the wake mode, the MI is populated by quasi-2D eddies with opposing senses of rotation that are shed from the junction corner region, similar to the wake behind a bluff body. Generally, a stagnation zone is present at the confluence apex. The wake mode is strong for cases when the difference between the horizontal velocities on the two sides of the MI, downstream of the stagnation zone, is not significant and the size of the stagnation zone is relatively large. In such cases, the transverse velocity shear is relatively small and the local velocity ratio $Vr(l) = U_1(l)/U_2(l)$ is close to 1, where l is the distance measured along the MI centerline and U_1, U_2 are the mean streamwise velocities in the two streams at a given streamwise location. For both modes, the spatial development of the quasi-2D MI eddies (e.g., their rates of growth), and thus the mixing between the two streams, are influenced by curvature effects [39, 42, 44].

The growth rate of a MI in the wake mode is generally smaller than that of a MI in the KH mode due to the lack of production of large-scale turbulence via mean transverse shear in horizontal planes. At natural confluences, both modes can coexist and affect the development of the MI eddies. Flow conditions, bed morphology and planform geometry will determine which mode is dominant. One important finding of the related study of Constantinescu et al. [20] was that the mean momentum flux ratio of the incoming streams is not always a good indicator of how the velocity ratio across the MI evolves downstream of the junction corner. The KH mode can be stronger than the wake mode at confluences with a momentum ratio of the two incoming streams close to unity, provided that the spatial development of the MI and the bathymetry features favor the acceleration of the flow on one side of the MI with respect to the other. The MI may be subject to curvature effects induced by mutual deflection of the confluent flows that reorients flow streamlines in the direction of the downstream channel. Moreover, curvature effects are influenced by the velocity relations between the two flows. For example, when the fast stream is on the outer side of a curved MI, mixing is inhibited (stably curved MI).

Besides the large eddies that populate the MI, of particular interest for mixing processes is the development of streamwise-oriented vortical (SOV) cells on one or both sides of the MI, which have been shown to strongly affect not only the redistribution of the streamwise velocity within the cross sections [54], but also to play a key role in mixing [2, 38, 43, 51, 54]. The loss of transverse momentum relative to the orientation of the MI produces an increase of pressure and super-elevation of the free surface near the junction apex. The raised free surface induces downward motion along the flanks of the MI and divergent flow near the bed, leading to the formation of a pair of counter-rotating SOV vortices. Their formation mechanism has similarities with that of the necklace vortices observed at the base of surface mounted obstacles [18, 31]. At asymmetrical confluences, the strength of the SOV cell on the tributary side of the confluence and downstream channel is generally larger and stronger (e.g., in terms of its cross-stream circulation) than the cell on the mainstream side especially for cases when the discharge of the tributary represents a significant fraction of the total discharge [18, 54]. SOV cells directly affect mixing through differential lateral advection of momentum over the depth of flow. Moreover, interaction between the SOV cells and the MI eddies can also result in enhanced mixing between the two streams [20]. Other factors, such as discordance between the bed elevation of the tributary and the main channel, bank irregularities, and large bed roughness can increase

the turbulent kinetic energy (TKE) near the channel boundaries within the confluence hydrodynamic zone, thereby increasing mixing rates [22]. Differences in density between the confluent flows may also contribute to patterns of mixing if buoyancy effects are large in relation to inertial forces [46].

If the difference in the fluid densities of the two streams is small and stratification effects can be neglected, the spatial development of the MI and the formation of large-scale vortical structures inside the confluence hydrodynamic zone are mainly controlled by the planform geometry, momentum/velocity ratio of the two streams, and bed morphology (e.g., see [16, 18, 20, 37, 43, 45, 48, 50, 52, 54–56]). Assuming the two streams have different inflow temperatures, the distribution of temperature downstream of the confluence apex depends to a large degree on how mixing between the two streams takes place downstream of the confluence apex [38, 54]. Differences in temperature influence physical habitat for aquatic organisms and can be particularly important in determining patterns of movement of mobile species within the main channel and tributaries as these organisms seek food, refuge, and locations to reproduce [49].

Most previous numerical investigations of flow and mixing at river confluences have used the Reynolds-Averaged Navier–Stokes (RANS) approach in which the eddy-viscosity/eddy-diffusivity model has to account for the influence of the turbulent eddies on the mean flow and mean transport [6, 8, 9, 46]. For example, numerical simulations of flow and mixing were performed for several natural confluences with discordant bed by Bradbrook et al. [9], Biron et al. [6] and Ramon et al. [46]. Over the last decade, large-eddy simulation (LES) techniques have become a powerful tool to investigate flows of relevance to river engineering and geosciences at laboratory and field scales [9, 21, 23, 26, 57]. In LES only the larger scales are directly resolved and a turbulence model is needed to account only for the effect of the unresolved scales on the resolved ones. Besides classical LES, Detached Eddy Simulation (DES) is another popular and robust LES-type method that can be used to predict and study the flow physics of turbulent flows at field conditions [57, 60]. LES and DES can capture the transfer of energy from the smaller to the larger scales (inverse energy cascade) that is essential for successful simulation of the dynamics of a MI in which quasi-2D eddies form [35, 58]. While some numerical investigations of flow at idealized and natural confluences have been performed using LES with wall functions [3, 9], for high-Reynolds-number flows, DES is preferred to LES with wall functions because it provides a more correct treatment of the near-wall flow and was shown to be more accurate [33]. Eddy-resolving 3D simulations also can be used to investigate interactions among large-scale turbulent structures and the effects of these structures on the mean flow and lateral mixing [26, 57]—phenomena that are difficult to evaluate in field and laboratory experiments [61]. Though LES was performed in the past for flow in natural confluence geometries [9], the meshes were too coarse and the numerical method too dissipative to accurately resolve the energetically important coherent structures in the flow, their dynamics and to understand how the main types of eddies affect the mixing process.

The increase in computing resources during the last decade have made possible investigating mixing processes in natural environments based on well-resolved simulations. In a series of recent studies, Constantinescu et al. [16, 18, 20] used highly-resolved DES calculations to investigate mean flow and turbulence structure at a confluence for which detailed data on the time-averaged velocity, temperature fields, and turbulence statistics are available [38, 53, 54, 61]. These simulations defined in detail the structure of the MI for the wake mode and the KH mode and the conditions under which SOV cells form in the vicinity of the MI. A major finding was that the cores of the SOV cells can be subject to large-scale aperiodic bimodal oscillations toward and away from the MI in the

region where the core of high velocity fluid from one stream approaches the MI. The formation of SOV cells is not dependent on the presence of a large junction angle and relatively strong SOV cells can form even in the case of parallel streams aligned with the downstream channel [20]. The numerical studies also showed that interaction between the SOV cells and the MI eddies is stronger for the wake mode than for the KH mode.

The present study uses DES to examine thermal mixing at a confluence with a concordant bed and natural bathymetry in which bank lines irregularities, spatial variations in bed topography, and flow curvature may significantly increase the three-dimensionality of the flow and affect thermal mixing in the confluence hydrodynamic zone. A main goal of the present paper is to understand the physical processes controlling lateral mixing at confluences with a concordant bed. In particular, the study seeks to understand how the main parameters characterizing the planform geometry and incoming flow characteristics in the two confluent streams (e.g., angles between the two tributaries and the main downstream channel, momentum flux ratio of the confluent streams) affect lateral mixing of two incoming streams with different temperatures. A second major goal of the present study is to describe the main mechanisms by which large-scale turbulence enhances thermal mixing at river confluences and how the importance of these mechanisms changes with the confluence planform geometry and momentum ratio of the two tributaries. Although the present study does not examine temperature stratification effects on mixing at confluences, it provides an important context for numerical-simulation investigations of stratification effects by exploring in detail mixing for the limiting case where temperature differences between the incoming streams are sufficiently small such that stratification effects can be ignored.

2 Numerical model

The DES model used to analyze thermal mixing at confluences has been used in previous studies of flow at confluences [16, 18, 20]. The viscous flow solver in the model solves the Navier–Stokes (momentum and continuity) equations in a time accurate way [13–16]. The eddy viscosity is provided by an eddy-resolving turbulence model (DES).

The low-Reynolds-number version of the Spalart–Allmaras (SA) RANS model is used as the base model in the DES module implemented in the viscous flow solver. No wall functions are used. The SA linear eddy-viscosity model is based on a transport equation for the modified eddy viscosity, $\tilde{\nu}$ [59, 60]. The SA version of DES is based on a modification of the length scale in the destruction term of the transport equation for the modified eddy viscosity solved in the RANS version of the SA model. The DES length scale is defined as $\tilde{d} = \min(d, C_{DES}\Delta)$, where d is the RANS length scale, Δ is a global measure of the size of the cell (e.g., $\Delta = \max(\Delta x, \Delta y, \Delta z)$) and the model constant is $C_{DES} = 0.65$. Away from the solid boundaries, the turbulence length scale is proportional to the local grid spacing, as in classical LES. Additional discussion of the SA DES model and implementation details can be found in Constantinescu and Squires [15].

An advection–diffusion equation for a conserved passive scalar (no source/sink terms) is solved for the nondimensional temperature, $TN = (T - T_{10})/(T_{20} - T_{10})$, where $T(x, y, z, t)$ is the temperature field, T_{10} is the temperature of the colder stream and T_{20} is the temperature of the warmer stream. This approach is similar to approaches used previous studies that looked at mixing between the two streams for cases where the density difference between the two streams was relatively small such that stratification effects on

mixing can be ignored (e.g., see [6, 9, 10]). The governing equation and methodology are the same as those described in Chang et al. [11]. On the solid surfaces (e.g., channel bottom) and on the free surface, the normal gradient of TN is set equal to zero (zero-flux boundary condition). At the outlet boundary, TN is obtained using extrapolation from the interior of the domain. The two extra parameters in the transport equation for TN are the Prandtl number, which is the ratio of the viscous diffusion to the thermal diffusion rate, and the turbulent Prandtl number, which is the ratio of the turbulent diffusion to the turbulent thermal diffusion rate.

A general description of the viscous flow solver is given by Chang et al. [11] and Kirkil et al. [30]. The 3D incompressible Navier–Stokes equations are integrated using a fully-implicit fractional-step method. The governing equations are written in generalized curvilinear coordinates and are discretized on a non-staggered structured grid. The convective terms in the momentum and scalar transport (e.g., nondimensional temperature) equations are discretized using a blend of fifth-order accurate upwind biased scheme and second-order central scheme. All other terms in the momentum, scalar/temperature transport and pressure-Poisson equations are discretized using second-order central differences. The discrete momentum (predictor step), scalar/temperature transport and turbulence model equations are integrated in pseudo-time using the alternate direction implicit (ADI) approximate factorization scheme. The time integration is done using a double time-stepping algorithm. The time discretization is second order accurate. The code is parallelized using Multiple Parallel Interface.

Validation of the DES solver for flow in curved channels with flat bed and natural bathymetry is reported by Constantinescu et al. [17, 19] and Koken et al. [34]. DES simulations conducted at similar Reynolds numbers to those of the present simulations and on meshes with a similar level of grid refinement were able to accurately capture the redistribution of the mean velocity by the cross-stream secondary flow and the turbulence structure inside the curved channel. Also relevant for the present investigation are the numerical simulations of the spatial development of a shallow mixing layer between two parallel streams conducted by Kirkil and Constantinescu [28] in a wide flat-bed channel. This test case corresponds to the limiting case of a confluence where the two incoming streams are aligned with the downstream channel. DES was able to accurately predict the streamwise variations of the shift of the mixing layer centerline and mixing layer width as well as the streamwise variation of the passage frequency of the quasi-2D mixing layer eddies and of the average horizontal dimensions of these eddies. Finally, the passive scalar transport module of the code that is used in the present study to compute the temperature distribution was validated by Chang et al. [11] in simple geometries.

In the present study, the DES solver is used to predict thermal mixing at confluences with a concordant bed for four different planform geometries labelled Case 1 to Case 4. Using the field measurements of Sukhdolov and Rhoads [61], Constantinescu et al. [16, 18] showed that DES was able to accurately capture the mean velocity and turbulent kinetic energy (TKE) distribution in several cross-sections situated within the confluence hydrodynamic zone for Case 1. The present paper reports additional validation data for the mean temperature field for Case 1, for which temperature measurements were obtained by Rhoads and Sukhdolov [54]. It provides direct validation of the solver for confluence problems involving scalar transport and is critical for establishing the accuracy of the temperature predictions. The other three simulations were conducted on meshes with similar levels of grid refinement and using the same nondimensional time step. Thus, the level of accuracy of the numerical predictions in the other three cases is expected to be comparable to that observed for Case 1.

3 Test cases and simulation set up

3.1 Description of test cases

In the present study the effects of incoming momentum ratio, channel curvature and angle between the two incoming streams on thermal mixing processes and spatial distributions of temperature are investigated based on four test cases. The flow hydrodynamics and turbulence structure for Case 1, Case 2 and Case 3 were analyzed by Constantinescu et al. [20]. The flow hydrodynamics and turbulence structure for Case 4 were analyzed by Constantinescu et al. [18]. The main parameters of the four cases are listed in Table 1.

Case 1 corresponds to flow conditions and bathymetry at the KR-CS confluence of Kaskaskia River (KR stream, $i = 1$) and Copper Slough (CS stream, $i = 2$) situated in Illinois, USA measured on May, 27 1998 by Rhoads and Sukhodolov [54] and Sukhodolov and Rhoads [61]. For this case, $U_{10} = 0.42$ m/s, $U_{20} = 0.46$ m/s, $Mr = 1.04$ and the angles between the KR stream (East tributary) and the CS stream (West tributary) are $\alpha_1 \approx 0^\circ$ and $\alpha_2 \approx 60^\circ$, respectively. The degree of bed discordance is negligible, the bathymetry contains a large scour hole with a maximum scour depth close to $3D$ (Fig. 1a) and the curvature of the inner bank relative to the channel width is close to 3.5. Using the mean velocity of the incoming streams, $U = 0.44$ m/s, as the velocity scale, and the mean channel depth in the downstream channel, $D = 0.36$ m, as the length scale, the Reynolds number of the flow is $Re = 166,000$ and the Froude number is $Fr = 0.24$. Simulation of flow hydrodynamics for Case 1 [20] showed that: (1) the velocity ratio across the MI remains close to one at most streamwise locations; (2) the wake mode is dominant inside the MI over the whole extent of the confluence hydrodynamic zone; (3) prominent SOV cells form on both sides of the MI (the SOV cells are visualized using the Q criterion proposed by Hunt et al. [25], in Fig. 2a). So, Case 1 is representative of asymmetric confluences with concordant beds where the wake mode dominates along the MI.

The bathymetry in Case 2 is obtained from that used in Case 1 by rotating the KR channel to make it parallel to the CS channel (Fig. 1b). As a result, $\alpha_1 \approx 60^\circ$ and $\alpha_2 \approx 60^\circ$. The widths of the confluence and downstream channel were left unchanged by the rotation, except for a short region situated close to the confluence apex. All the main features of the bathymetry and bank lines were preserved as a result of the rotation (Fig. 1a, b). The other flow parameters are identical to those used in Case 1, including the momentum ratio of the incoming streams, the Re and Fr numbers. Simulation of flow hydrodynamics for Case 2 [20] showed that: (1) the MI moves toward the west bank compared to Case 1; (2) the local velocity ratio across the MI increases significantly with

Table 1 Main geometrical and flow parameters of the four test cases

Case	α_1 ($^\circ$)	α_2 ($^\circ$)	Mr
1	0	60	1.04
2	60	60	1.04
3	0	0	1.04
4	0	60	5.4

Case 1 corresponds to Case 1 in Constantinescu et al. [18] and Constantinescu et al. [20]. Cases 2 and 3 correspond to Cases 2 and 3 in Constantinescu et al. [20], respectively. Case 4 corresponds to Case 2 in Constantinescu et al. [18]

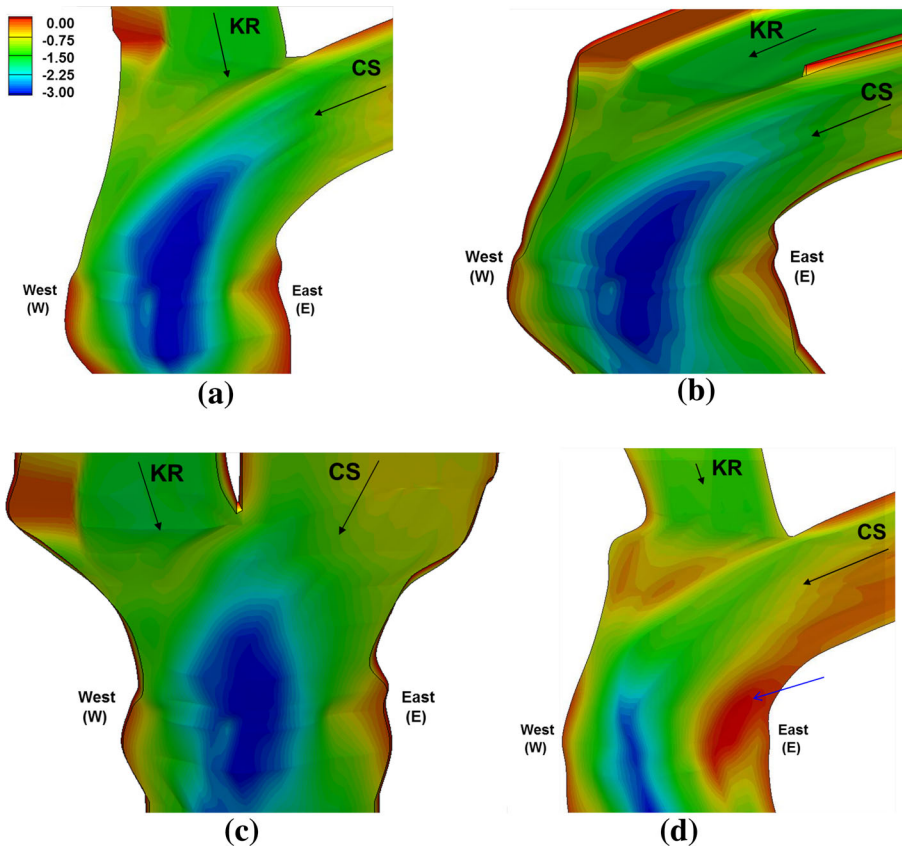


Fig. 1 Confluence geometry and bathymetry contours for: **a** Case 1; **b** Case 2; **c** Case 3; **d** Case 4. The bathymetry is visualized using nondimensional bed elevation values, z'/D , where $z'/D = 0$ corresponds to the free surface

the distance from the junction corner, such that the KH mode becomes dominant within the downstream part of the MI; (3) a strong SOV cell is only observed on the CS (East) side of the MI (Fig. 2b). As the MI shifts toward the outer (west) bank, high velocity fluid on the outside of the curved MI damps the growth of the quasi-2D MI eddies. One of the main reason the wake mode is weak in Case 2 is that no flow stagnation occurs close to the junction corner because of the streamlined shape of this corner. So, Case 2 is representative of confluences with concordant beds, with parallel streams that form a large angle with the downstream channel, and where the KH mode progressively increases in dominance along a stably-curved MI.

The bathymetry in Case 3 is obtained from that used in Case 2 by rotating the centerline of both incoming streams such that both upstream channels are aligned with the downstream channel (Fig. 1c). As a result, $\alpha_1 \approx 0^\circ$ and $\alpha_2 \approx 0^\circ$. The other flow parameters are identical to those used in Case 1 and Case 2. Simulation of flow hydrodynamics for Case 3 [20] showed that, similarly to Case 2, the KH mode becomes more pronounced with increasing distance from the junction corner, but that the MI is situated close to the centerline of the downstream channel (Fig. 2c). A fairly coherent SOV cell forms on the

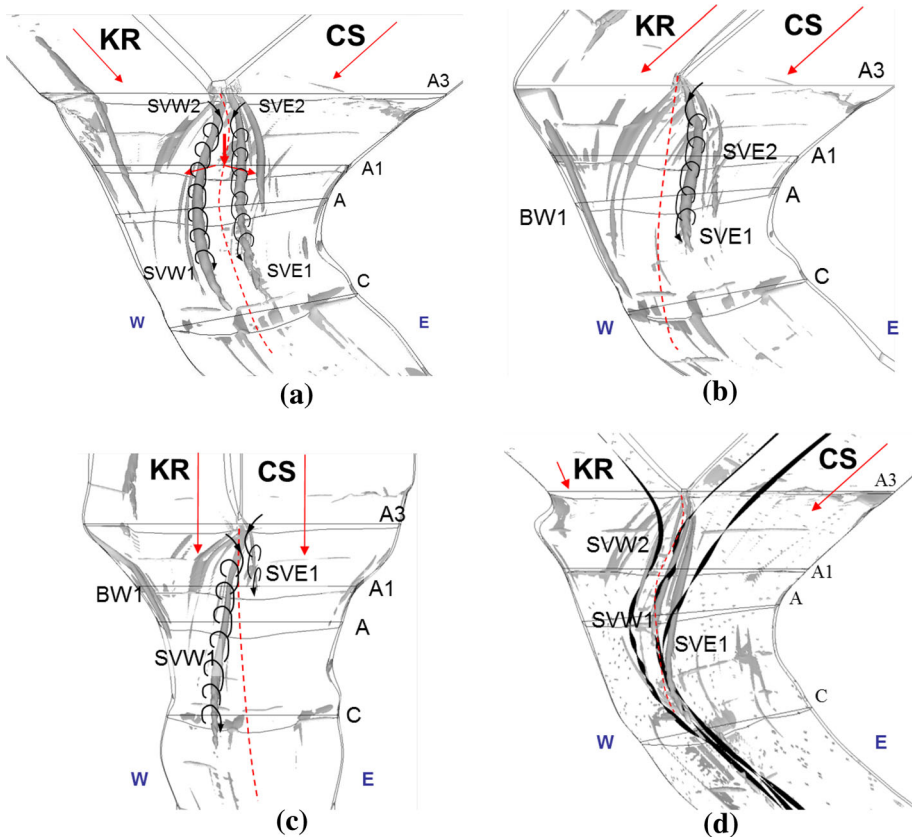


Fig. 2 Visualization of the main vortical structures in the mean flow using a Q iso-surface ($Q = 10$). **a** Case 1; **b** Case 2; **c** Case 3; **d** Case 4. The *dashed red line* shows the approximate position of the MI centerline. SVE1 and SVE2 are the SOV cells on the East (E) side of the confluence. SVW1 and SVW2 are the SOV cells on the West (W) side of the confluence. BW1 is a SOV cell forming at the West bank. The 3D ribbons in frame **d** show the large rotational capacity of the main SOV cells. Frames **a–d** are reproduced or adapted from Constantinescu et al. [18, 20]

KR side of the MI. At a given streamwise location, the local velocity ratio values are less than those observed for Case 2 and the KH mode remains relatively weak compared to Case 2. Moreover, the curvature of the MI centerline is small and no flow stagnation occurs close to the upstream junction corner. So, Case 3 is representative of confluences with concordant beds, with parallel streams that are closely aligned with the downstream channel, and for which the effects of curvature on the spatial development of the MI eddies are negligible. Although Case 2 and Case 3 simulations include the same bathymetry as that for Case 1, Constantinescu et al. [20] showed that the spatial development of the MI and large-scale flow structures within the confluence is qualitatively similar in simulations conducted with same planform geometry but with a flat bed versus a deformed bed. Thus, mixing should not be strongly influenced by bathymetric conditions and instead appears to depend mainly on the planform geometry and momentum ratio. Nevertheless, localized effects caused by rapid bathymetry changes could be locally important (e.g., where a very deep scour hole is present) [4, 50].

The flow conditions and bathymetry in Case 4 correspond to those measured at the KR-CS confluence on May, 26 1999 by Rhoads and Sukhodolov [56]. For this case, $U_{10} = 0.19$ m/s, $U_{20} = 0.45$ m/s, $Mr = 5.4$ and the angles between the downstream channel with the KR (East tributary) and the CS (West tributary) streams are $\alpha_1 \approx 0^\circ$ and $\alpha_2 \approx 60^\circ$, respectively. The mean flow depth in the downstream channel is about two-thirds of that in Case 1. Similar to Case 1, a large scour hole extends downstream of the confluence apex. Additionally, a submerged bar is present along the east bank (Fig. 1d). Using the mean velocity of the two incoming streams and the mean flow depth in the downstream channel, the Reynolds number is 77,000 and the Froude number is 0.22. As $Mr \gg 1$ in Case 4, the KH mode is expected to be dominant inside the MI starting at the upstream junction corner—a condition confirmed by simulation of flow hydrodynamics for Case 4 (Case 2 in [18]). Simulation results also show that, similar to Case 2, strongly coherent SOV cells form only on the CS side of the MI because of the large velocity magnitudes within the core of high speed flow entering the confluence from the CS side and the relatively large angle of the CS flow with the MI centerline (Fig. 2d).

3.2 Simulation set up

In all four cases, the computational domain was meshed with close to 5 million cells, of which about 30 points were used to resolve the flow over the channel depth. Based on field measurements of the bed material of the KR-CS confluence, the channel bed and banks were treated as rough surfaces with a mean value of the roughness height equal to 0.01 m. The velocity components at the entrance in the two incoming channels were obtained from two precursor simulations that provided the total instantaneous velocity fields corresponding to fully-developed turbulent channel flow (see [18]). At the downstream end of the main channel, a standard convective boundary condition was used [57]. Given the relatively low value of the physical Froude number in all 4 cases ($Fr < 0.25$), the free surface was modeled as a shear-free rigid lid. Though simulations using the rigid lid approximations do not capture the deformations of the free surface, they predict a nonuniform distribution of the pressure on the free surface that is consistent with the main features observed at the free surface of the confluence (e.g., region of superelevation close to the confluence apex), as also discussed by Constantinescu et al. [16].

The nondimensional temperature (TN) of the colder KS stream was set equal to 0 over the whole inflow section. At the inflow section of the warmer CS stream, TN was set equal to 1. The temperature gradient in the normal direction to the other surfaces of the computational domain (channel bottom, free surface) was set equal to 0 (zero heat flux). Thus, TN is expected to vary between 0 and 1 in the interior of the computational domain. The molecular Prandtl number was assumed to be equal to 7 while the turbulent Prandtl number was assumed to be equal to 1. This value corresponds to thermal diffusion in water at around 15–20 °C. The maximum temperature difference, $T_{20} - T_{10}$, during the field experiment corresponding to Case 1 was close to 2.5 °C. The dimensional temperatures in the two incoming streams, T_{10} and T_{20} , correspond to $TN = 0$ and $TN = 1$ in the nondimensional plots (e.g., see Fig. 8). This information is needed only when the nondimensional mean (time-averaged) temperature field, TNM, needs to be converted to a dimensional temperature field, T, such that direct comparison with field measurements is possible.

The results for the four cases are presented in nondimensional form, with $U = 0.44$ m/s and $D = 0.36$ m as the velocity scale and length scale, respectively. The time step was

0.1 D/U in all four simulations. Statistics were collected over a time interval equal to 900 D/U. Statistics were checked for convergence.

4 Effect of coherent structures on thermal mixing processes

Constantinescu et al. [18, 20] have shown that, regardless of whether the KH mode or the wake mode dominates, the MI eddies can be described as quasi-2D eddies extending over the whole flow depth whose axes are close to vertical. The main mixing mechanism driven by which the colder fluid from the KR stream mixes with the warmer fluid from the CS stream in the MI region is large-scale interpenetration by the quasi-2D eddies. This process is illustrated in Fig. 3 for Case 1, where the wake mode dominates inside the MI. In a good approximation, interpenetration can be considered to be close to uniform over the flow depth as the isotherm surface, $TN = 0.5$, is close to vertical in Fig. 3 in regions where the SOV cells are not situated close to the MI or sharp bathymetry variations are not present.

The average size of the packets of lower temperature fluid penetrating on the higher temperature side is proportional to the average size of the MI eddies (Fig. 3). The same is true for the packets of higher temperature fluid penetrating on the lower temperature side. So interpenetration is expected to be a major mechanism for thermal mixing when the average size of the cores of the MI eddies and their coherence (e.g., as measured by the circulation in a horizontal plane) are high. For MIs where the KH mode is very strong,

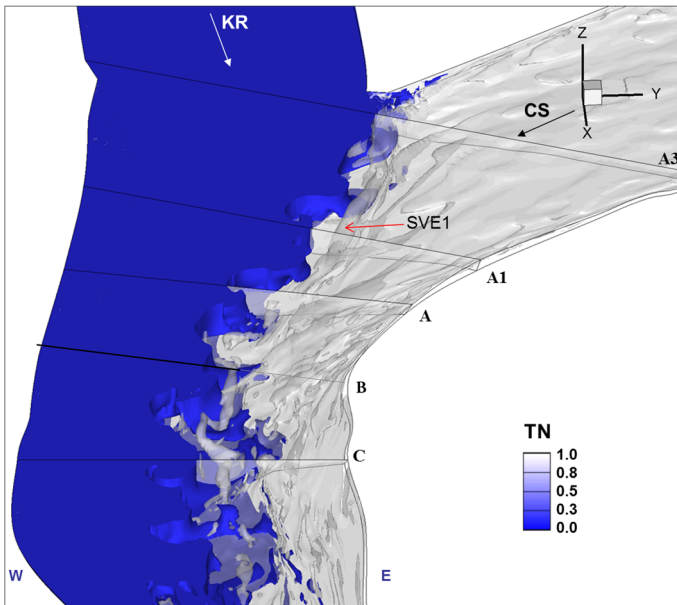


Fig. 3 Visualization of the mixing between the KR stream (blue) and the CS stream (white) using an instantaneous iso-thermal contour, $TN = 0.5$. The 3-D surface with $TN = 0.5$ is used to visualize the engulfing motions associated with the MI eddies which are an important mechanism for mixing (e.g., via interpenetration) between the two streams. Also shown are the coherent structures in the instantaneous flow field on the CS side using a Q isosurface ($Q = 5$). The eddies are shown in gray (e.g., see arrow pointing toward SVE1)

pairing of successive quasi-2D eddies is responsible for the growth in the coherence and size of the MI eddies away from the upstream junction corner. The size of the MI eddies also increases with the distance from the junction corner in MIs where the wake mode is dominant. For example, in Case 1, the average size of the MI eddies and the lateral size of the intrusions of higher temperature fluid on the East side of the confluence can be as high as 3 times the average flow depth in the downstream channel. As will be discussed later, this value is lower, but still comparable, to the size of the largest eddies and intrusions observed in Case 4, where the KH mode is very strong. However, for MIs where the wake mode is dominant, there is no mechanism that can induce an increase in the coherence of the MI eddies as they are advected downstream. Thus, one expects interpenetration will play a more important role at confluences where the KH mode is very strong.

At very large distances from the upstream junction corner, interpenetration decreases in importance. At MIs where the wake mode dominates, the coherence of the MI eddies decays sufficiently such that their capacity to create intrusions via their rotational velocity becomes negligible. The same effect happens for a MI where the KH mode dominates. In the classical case of free (deep) mixing layers, the size and coherence of the KH billows

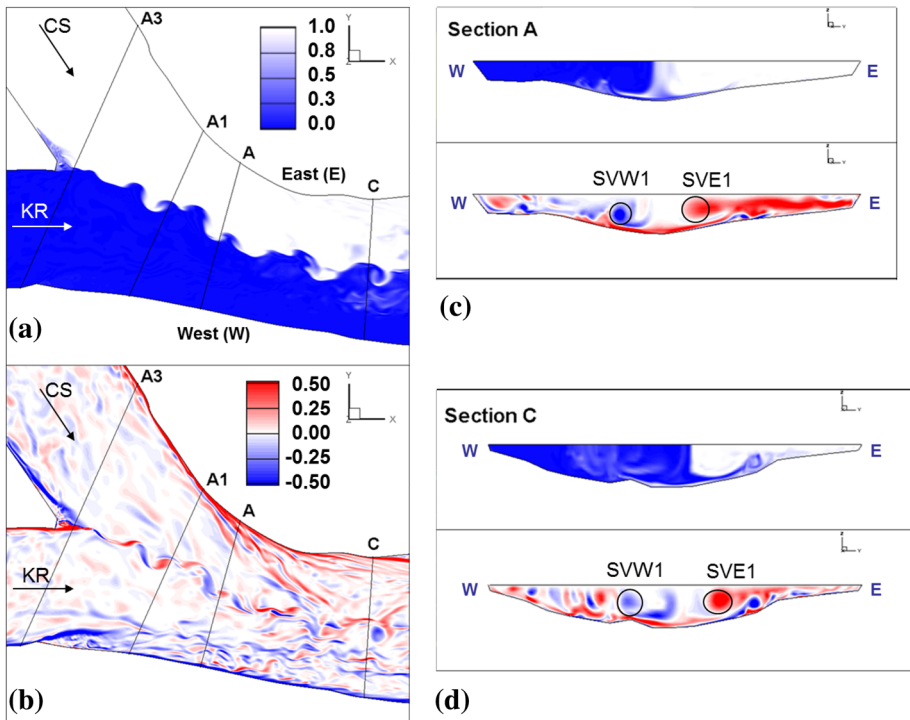


Fig. 4 Visualization of thermal mixing and vortical flow structure in Case 1. The nondimensional temperatures of the incoming flow in streams KR and CS are $TN = 0$ and $TN = 1$, respectively. **a** Instantaneous nondimensional temperature, TN , in a horizontal surface situated $0.1 D$ below the free surface; **b** instantaneous nondimensional vertical vorticity, $\omega_z(D/U)$, in a horizontal surface situated $0.1 D$ below the free surface; **c** instantaneous nondimensional temperature, TN , and streamwise vorticity, $\omega_x(D/U)$, in section A; **d** instantaneous nondimensional temperature, TN , and streamwise vorticity, $\omega_x(D/U)$, in section C. The black circles visualize the cores of the main SOV cells. Frame **b** and part of frame **c** are adapted from Constantinescu et al. [15, 16, 17]

increases continuously with the distance from the origin of the mixing layer. However, growth of structures is inhibited (e.g., vortex pairing is not observed at large distances from the junction corner) for mixing layers developing in shallow environments over a no-slip bottom boundary [3, 28, 29], which is the case of MI at river confluences. As a result, at a certain point these structures start losing their coherence. Thus, regardless of which mode dominates within the MI, mixing via interpenetration of coherent structures should be an important mechanism for thermal mixing within confluences with concordant beds only over a finite distance from the upstream junction corner.

The results also illustrate the effect of the SOV cells on thermal mixing (Fig. 3). Near locations where the core of a strong SOV cell is situated close to the MI (e.g., between sections A3 and A1 for cell SVE1), the isotherm surface orientation tends to deviate from the vertical and some isolated patches of higher temperature fluid are observed on the East side of the MI. The types of interactions between the SOV cells and the MI will be discussed in detail later for each test case.

The nondimensional temperature and vertical vorticity distributions illustrate the direct effect of the MI eddies on the instantaneous temperature field for Case 1 (Fig. 4a). Given that a relatively large stagnation zone is present at the upstream junction corner, interactions between the separated shear layers on the two sides of this zone of separated fluid are strong. This results in the development of energetic counter-rotating billows mid-way between sections A3 and A1 (Fig. 4b). Variation in the coherence of the MI eddies between sections A1 and C is fairly small. Thus, the intensity of interpenetrations and the average size of the mushroom-like intrusions of fluid from one side of the confluence into the other along the MI are comparable within the confluence hydrodynamic zone for Case 1. As expected, the stagnation zone contains fluid with a temperature close to the average temperature of the two streams. Several packets of fluid with temperatures significantly different than that of the surrounding flow are observed close to section C in both streams. These packets are generated by the shear layer induced by the strong curvature of the inner (East) bank and the separated shear layer originating close to section A3 at the West bank. Large scale eddies form in the downstream part of these shear layers and these eddies interact with the MI close to section C (Fig. 4b).

The effect of the SOV cells on mixing in Case 1 is illustrated based on the instantaneous flow distributions of the nondimensional streamwise vorticity and temperature distributions in cross sections A and C (Fig. 4c, d). The main SOV cells on the two sides of the MI rotate in opposite directions and induce a downward movement of the fluid within the MI. Once this fluid reaches the bed, it is advected away from the MI toward the banks. This pattern of fluid motion produces near-bed intrusions of cooler fluid on the East side of the confluence and of warmer fluid on the West side. Examination of animations of the temperature field shows that the penetration length of the near bed-intrusion is not constant in time on either side of the MI. These temporal variations are particularly large in the region where the strength of the bimodal oscillations of the SOV cells is the largest (e.g., between sections A1 and B for Case 1, see discussion in [18]). At a given streamwise location, the length of the intrusion increases when the core of the main SOV cell moves closer to the MI (the SOV cell is in the mixing interface mode) and decreases when the SOV cell is situated farther from the MI (the SOV cell is in the bank mode). The role of the bimodal oscillations in modulating the strength of the near-bed intrusion of fluid with a temperature that is higher or lower than that of the fluid into which it penetrates is the same in the other test cases where strongly-coherent SOV cells form on one or both sides of the MI.

Given that stratification effects are neglected, intrusions of low temperature fluid into the higher temperature CS side of the confluence and of high temperature fluid into the lower temperature KR side should be close to equal if the coherence of the SOV cells on the two sides of the interface and their position relative to the MI are comparable. Constantinescu et al. [16] have shown that the circulations of SVE1 and SVW1 are equal at sections A1 and A (Fig. 4c), whereas the circulation of SVE1 is about 40 % lower than that of SVE1 at section C (Fig. 4d). This explains why the penetration lengths of the tongues of lower/higher temperature fluid from each stream into one another are roughly the same at section A, but that the intrusion of low temperature fluid on the CS side is much larger than that of higher temperature fluid on the KR side at section C. The coherence of SVE1 at section C is sufficiently high to induce the periodic ejection of patches of near-bed lower-temperature fluid from the bottom boundary layer. This mechanism contributes to the rapid mixing of colder -temperature fluid extracted by the SOV cell from the MI region with the surrounding fluid. The secondary SOV cell on the CS side, SVE2, further contributes to the advection of this fluid toward the East bank (the primary and secondary SOV cells are always co-rotating vortices).

Entrainment of fluid by the MI eddies is a major mechanism for thermal mixing in Case 2, in which the wake mode is weak. The gradual increase of the mean shear along the MI between the junction corner and section A1 amplifies the KH mode relative to the wake mode. Well-defined co-rotating quasi-2D eddies develop until midway between sections A1 and A (Fig. 5a). The average size of these eddies is much smaller than that of the counter-rotating eddies advected inside the MI in Case 1. As a result, the average size of the temperature intrusions on each side of the MI is smaller in Case 2 compared to Case 1. Downstream of section A1, the large MI eddies are subject to stretching. More importantly, curvature effects damp the natural growth of the MI eddies. These effects produce irregular deformations of the temperature interface and an overall decay in the average size of the intrusions between sections A1 and B (Fig. 5a).

Large-scale intrusions of warmer fluid are observed between sections B and C near the free surface. These intrusions are driven by the advection of large-scale eddies into the MI.

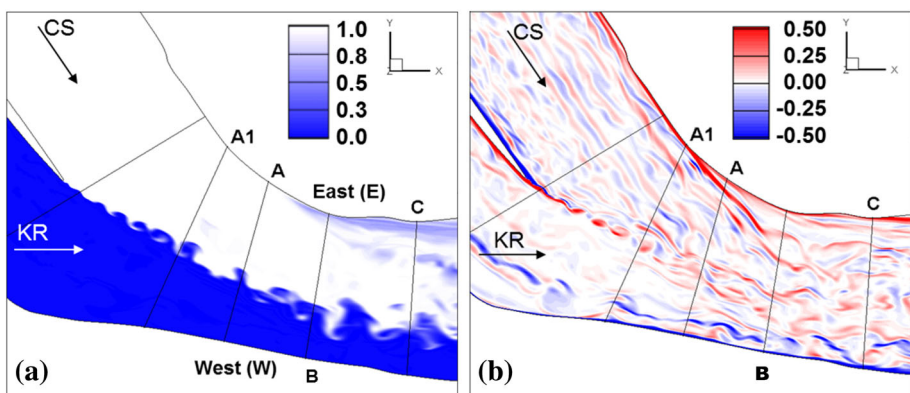


Fig. 5 Visualization of thermal mixing and vortical flow structure in Case 2. The nondimensional temperatures of the incoming flow in streams KR and CS are $TN = 0$ and $TN = 1$, respectively. **a** Instantaneous nondimensional temperature, TN , in a horizontal surface situated $0.1 D$ below the free surface; **b** instantaneous nondimensional vertical vorticity, $\omega_z(D/U)$, in a horizontal surface situated $0.1 D$ below the free surface. Frame **b** is adapted from Constantinescu et al. [20]

These eddies are generated inside the shear layer induced by strong inner bank curvature near section A1 (Fig. 5b). Due to their high momentum, the penetration length of these eddies is in some cases quite large (e.g., about half the local width of the KS side of the confluence, Fig. 5a). The large-scale turbulence generated by West bank irregularities near section A3 do not play any important role in thermal mixing as these eddies are advected in a region containing mostly cold fluid from the KR stream. The same is true for vortex BW1 (Fig. 2b) that forms along the West bank as a result of deflection of the core of high streamwise velocities from the incoming KR stream by this bank.

The nondimensional temperature distributions in cross sections A1 and A (not shown) do not display any near-bed intrusions of high-temperature fluid on the KR side of the MI. Meanwhile strong near-bed intrusions of colder-temperature fluid occur between sections A1 and B on the CS side of the confluence (see also Fig. 6c in [20]). These features of the temperature distributions in the cross sections are fully consistent with the SOV cell structure in Case 2. The coherence of the SOV cells on the West side of the MI is low while a strongly coherent SOV cell, SVE1, is present on the East side (Fig. 2b). Moreover, the core of SVE1 is subject to strong bimodal oscillations between sections A1 and B. Similar, to the mechanism described for Case 1, the co-rotating SVE1 and SVE2 cells transport

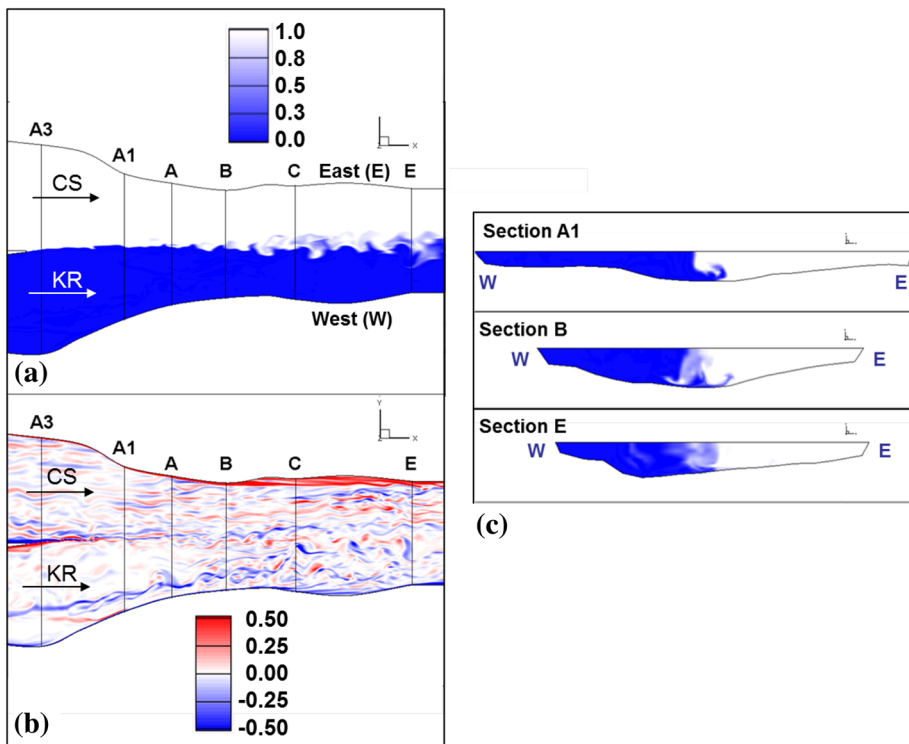


Fig. 6 Visualization of thermal mixing and vortical flow structure in Case 3. The nondimensional temperatures of the incoming flow in streams KR and CS are $TN = 0$ and $TN = 1$, respectively. **a** Instantaneous nondimensional temperature, TN , in a horizontal surface situated $0.1 D$ below the free surface; **b** instantaneous nondimensional vertical vorticity, $\omega_z(D/U)$, in a horizontal surface situated $0.1 D$ below the free surface, **c** instantaneous nondimensional temperature, TN , in sections A1, B and E. Frame **b** is adapted from Constantinescu et al. [20]

near-bed cooler fluid toward the East bank. Downstream of section B the flow shoals near the East bank and the colder near-bed fluid approaches the free surface, producing a region of cooler fluid bordered by the shear layer, which originates at section A1, and the East bank (Fig. 5a).

In Case 3 the strength of the KH mode, the size of the quasi-2D MI eddies, and mixing by interpenetration increase fairly monotonically over distance from the upstream junction corner. Given that no stagnation zone forms at the junction apex, the wake mode is weak despite the fact that $Mr \approx 1$. The large intrusion of colder temperature fluid on the CS side

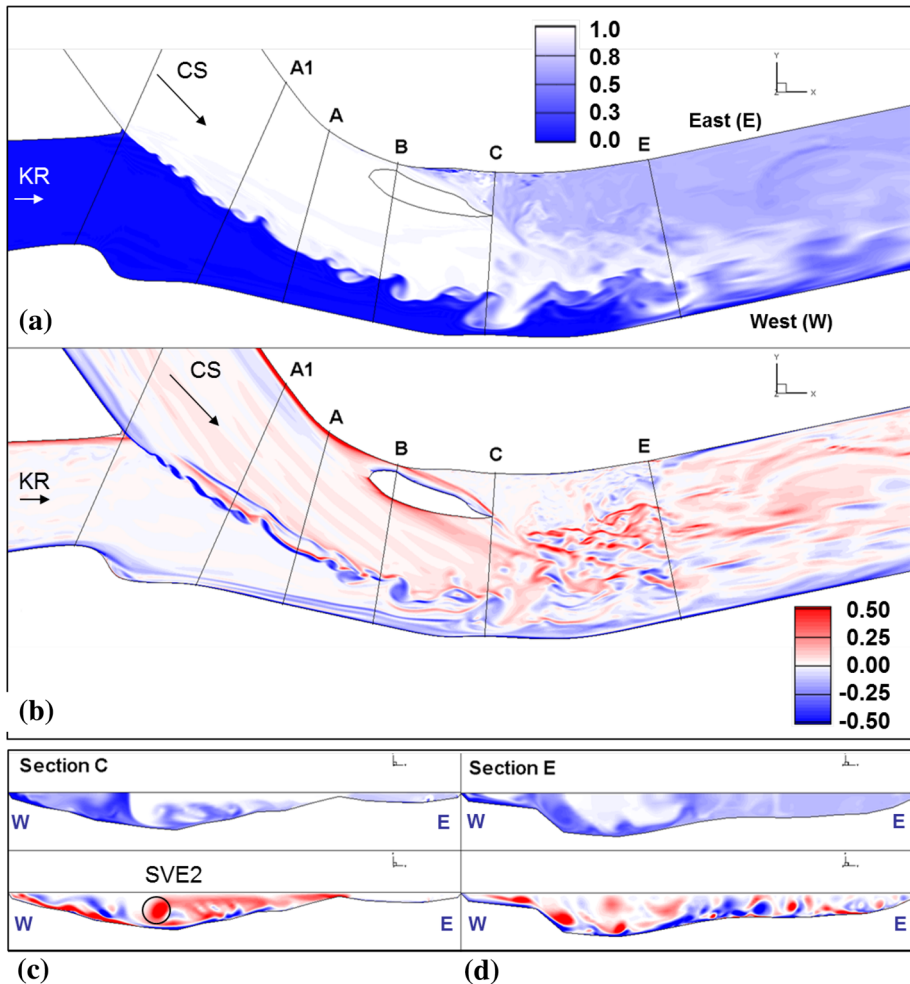


Fig. 7 Visualization of thermal mixing and vortical flow structure in Case 4. The nondimensional temperatures of the incoming flow in streams KR and CS are $TN = 0$ and $TN = 1$, respectively. **a** Instantaneous nondimensional temperature, TN , in a horizontal surface situated $0.1 D$ below the free surface; **b** instantaneous nondimensional vertical vorticity, $\omega_z(D/U)$, in a horizontal surface situated $0.1 D$ below the free surface, **c** instantaneous nondimensional temperature, TN , and streamwise vorticity, $\omega_s(D/U)$, in section C; **d** instantaneous nondimensional temperature, TN , and streamwise vorticity, $\omega_s(D/U)$, in section E. Frame **b** is adapted from Constantinescu et al. [18]

at section A1 (Fig. 6c) is due to the small, but highly coherent, SVE1 cell (Fig. 2c). The absence of a secondary SOV cell on the East side of the MI restricts the zone of mixed fluid to the vicinity of the MI rather than extending close to the bank, as occurred in Cases 1 and 2. Downstream of section A, the coherence of the main SOV cell on the East side is negligible (Fig. 2c); thus, only weak near-bed intrusions of lower temperature fluid occur on the CS side of the confluence along the downstream part of the MI. What appears in section B to be an intrusion of colder fluid on the CS side (Fig. 6c) is in fact colder fluid being advected from upstream. Meanwhile, near bed intrusions of warmer fluid on the KR side of the interface are observed between sections A and C (Fig. 6c). They are driven by the main SOV cell on the West side of the MI. Given that the core of SVW1 is not subject to bimodal oscillations, these intrusions are weaker and characterized by a lower degree of temporal variation in the penetration length compared to the East side intrusions present in Cases 1 and 2.

The energetic eddies generated at the West bank have a significant influence on thermal mixing as these eddies move downstream and interact with the MI eddies (see Fig. 6b between sections C and E). As a result, the size of the horizontal intrusions of warmer/colder fluid and mixing by interpenetration are enhanced between sections C and E on the KR side of the confluence (Fig. 6a). Moreover, the high three-dimensionality of these energetic eddies is responsible for enhancement of local mixing within the MI and along its West boundary. This process explains the absence of a sharp temperature interface in the instantaneous temperature field at section E (Fig. 6c); rather, the MI contains fluid with a temperature that is close to the mean temperature of the two incoming streams.

In Case 4, the size of the MI quasi-2D eddies and the mixing by interpenetration of these eddies increase fairly monotonically with the distance from the confluence apex to section C. At and downstream of section C, the mean flow becomes highly three-dimensional on the CS side of the confluence because the submerged bar at this location has a strong influence on fluid motion (Fig. 7a, b). Compared to Case 3, the KH mode is much stronger at all streamwise locations and, on average, two vortex pairing events take place as MI eddies are advected between sections A1 and C [19]. As a result, the average size of the intrusions of warmer/colder fluid on the East/West side of the MI is larger in Case 4 compared to Cases 2 and 3 (Figs. 5a, 6a, 7a). In Case 4, the widths of these intrusions around section C can be as high as 5–6 times the mean flow depth in the downstream channel. Deflection of the MI centerline by the high momentum flow in the CS stream leads to intrusions downstream of section C that extend to the West bank. Thus, downstream of section C, the temperature of the fluid on the KR side of the MI is everywhere greater than that of the incoming fluid in the KR stream. Instantaneous nondimensional temperature distributions at sections C (Fig. 7c) and E (Fig. 7d) show that substantial thermal mixing has occurred on the West side of the MI. This mixing is driven by intrusions of large patches of warm fluid that penetrate until close to the West bank.

Although near-bed intrusions are observed between sections A3 and A on both sides of the MI, the intrusions on the CS side are much stronger than those on the KR side (not shown). Similar to conditions for Case 1, the co-rotating SOV cells on the CS side (SVE1 and SVE2 in Fig. 2d) transport the cooler temperature fluid from the KR side toward the East bank. Between sections A3 and A, the instantaneous temperature field is characterized by a fairly sharp vertical interface from the free surface to near the bed, where intrusions driven by the bimodal oscillations of SVE1 occur. Similar to Case 1, the wake mode dominates inside the MI, but strong SOV cells are present in the vicinity of the MI.

Marked differences in thermal mixing compared to the other 3 cases are observed in Case 4 downstream of section B on the CS side of the MI. One reason is the presence of the

secondary SOV cell, SVE2, in the vicinity of the MI. Downstream of section A, the coherence of SVE1 is lost, while SVE2 maintains its coherence and approaches the MI. The coherence of SVE2 remains relatively large until section C. This cell advects cooler temperature fluid from the KR side toward the East bank (Fig. 7c). Another important feature of the temperature distribution downstream of section C is the presence of a region occupying most of the CS side of the confluence containing fluid with a temperature that is significantly less than that of the incoming fluid in the CS stream (Fig. 7a, d). This region occupies most of the flow depth downstream of section E (Fig. 7d). The main mechanism that is responsible for the formation of this region of fluid of fairly uniform temperature is

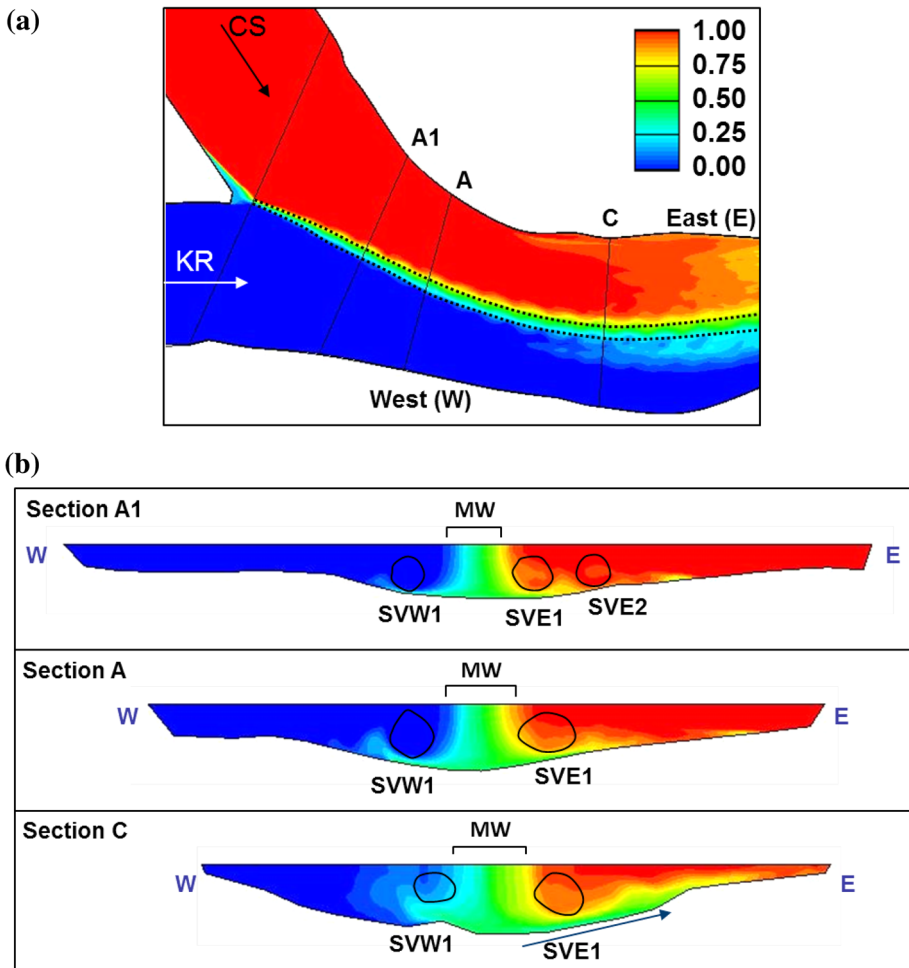


Fig. 8 Visualization of thermal mixing in the mean flow for Case 1. The nondimensional time-averaged temperatures of the incoming flow in streams KR and CS are $T_{NM} = 0$ and $T_{NM} = 1$, respectively. **a** Nondimensional time-averaged temperature, T_{NM} , in a horizontal surface situated $0.1 D$ below the free surface; **b** nondimensional time-averaged temperature, T_{NM} , in sections A1, A and C. Dotted lines show approximate extent of the thermal MI close to the free surface. The black circles visualize the cores of the main SOV cells in the mean flow

that the flow separates over most of the water column past the elongated bar of deposited sediment. A region of slowly moving fluid forms behind the bar. Most of the lower temperature fluid on the CS side of the confluence downstream of section C originates in the near-bed intrusions of KR fluid extracted from the MI region by SVE1 and SVE2. As it is advected downstream by the mean flow this cooler fluid moves laterally, beneath the core of high-speed fluid containing mostly fluid from the incoming CS stream. Eventually, this cooler fluid is injected into the recirculating zone in the lee of the bar along the East bank. The large energetic eddies observed between sections C and E in Fig. 7b, d are very effective in locally mixing the flow, which accounts for the relatively uniform temperature distribution of the flow on the CS side downstream of section E.

5 Mixing and time-averaged temperature fields

The spatial pattern of mixing at KRCS is revealed through examination of the time-averaged temperature fields at the confluence. The distribution of the mean nondimensional temperature field for Case 1 shows that the mean position of the MI, defined by a narrow zone of strong lateral gradient in temperature, generally follows the deepest part of the channel (i.e., it is situated over the scour hole, see also Fig. 1a) and the isotherms are close to vertical near the free surface (Fig. 8). The width of the MI close to the free surface increases slightly with distance from the upstream junction corner. Persistent interpenetration of fluid from the two streams is evident in the mean temperature field. In particular,

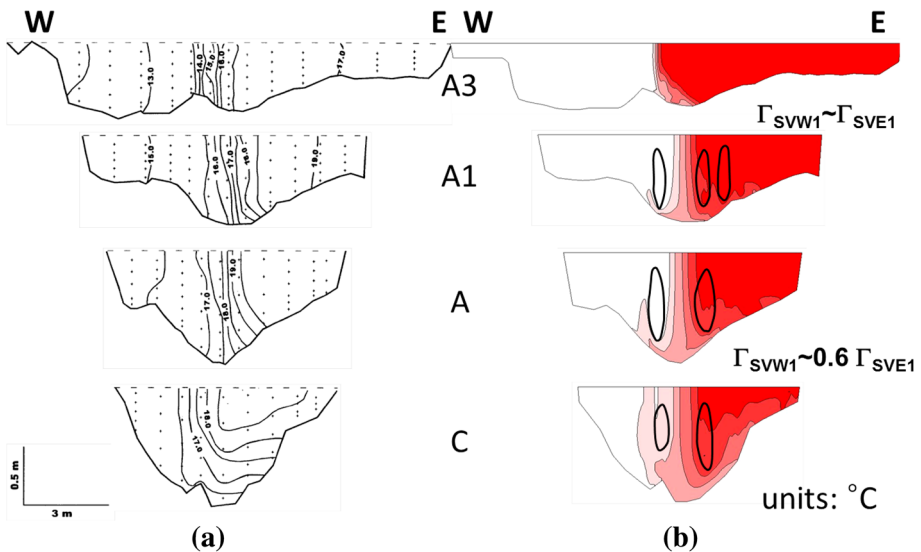


Fig. 9 Distribution of temperature, T ($^{\circ}\text{C}$), in several cross sections (A3, A1, A and C) for Case 1. **a** Field experiment; **b** DES predictions. The scale is distorted in the vertical direction (aspect ratio is 1:0.208). The difference between the iso-temperature lines in both frames is $0.5\text{ }^{\circ}\text{C}$. The initial temperatures of the incoming KR and CS streams on the West and East side of the confluence are visualized with *white* and, respectively, *red color*. The *black elliptical shapes* in frame **b** visualize the extent and relative position of the main SOV cells (SVW1, SVE1, SVE2) in the cross section. Frame **a** is reproduced from Rhoads and Sukhodolov [54]. Information in **b** is equivalent to that shown in Fig. 8b except for the aspect ratio that was modified to allow comparison with field data

spreading of the isotherms in the near-bed region occurs where fluid from one of the streams is advected into fluid from the other by the SOV cells. Downstream of section A1, the penetration length of the near-bed intrusion on the East side of the MI is larger than that of the near-bed intrusion on the West side because the strength of the SOV cell on the East side of the confluence is stronger than the cell on the West side. Within the confluence, the penetration length of the intrusion on the West side is less than two times the mean flow depth in the downstream channel. As a result, the temperature of most fluid on the KR side of the confluence is close to that of incoming flow in the KR stream. The enhanced circulation of SVE1 compared to SVW1 and the shoaling of flow near the East bank of the downstream channel are the main reasons why, downstream of section B, the penetration length of the near bed intrusion is much larger on the East side of the confluence compared to the West side. As a result, downstream of section C, the temperature of most of the fluid

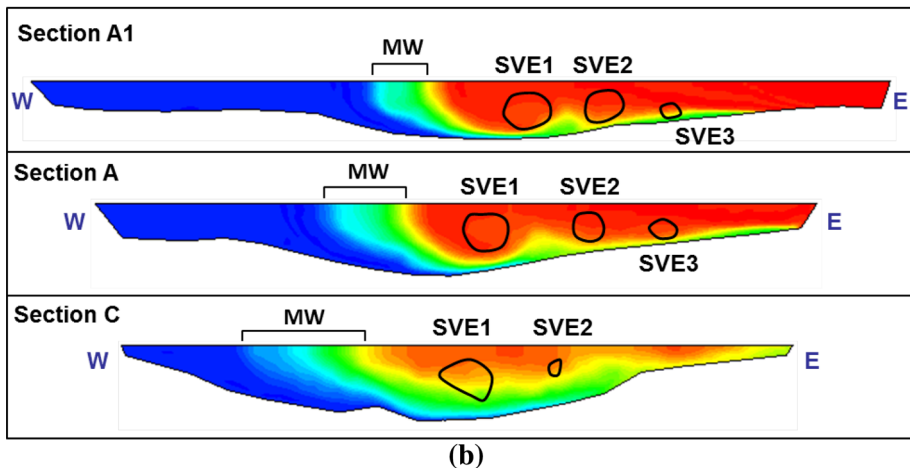
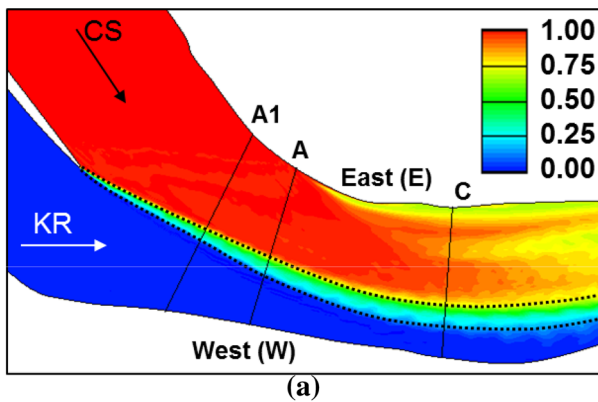
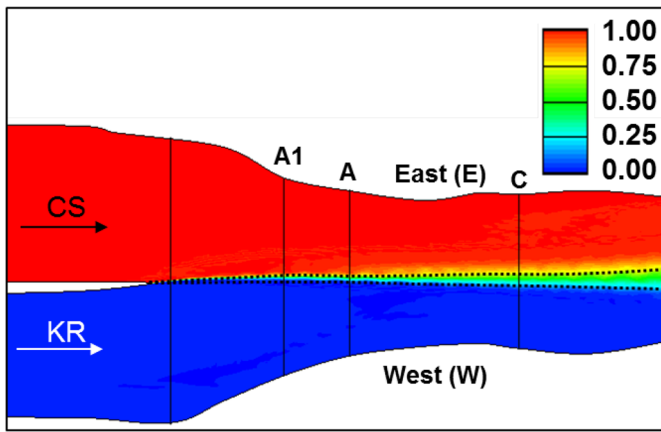


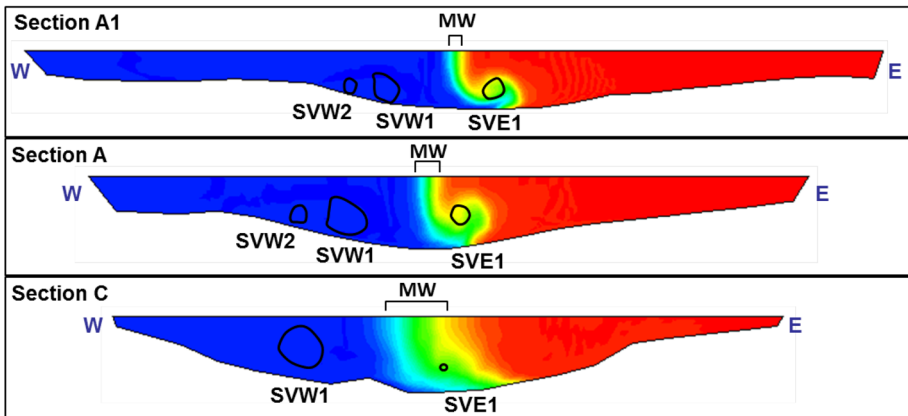
Fig. 10 Visualization of thermal mixing in the mean flow for Case 2. The nondimensional time-averaged temperatures of the incoming flow in streams KR and CS are $TNM = 0$ and $TNM = 1$, respectively. **a** Nondimensional time-averaged temperature, TNM , in a horizontal surface situated $0.1D$ below the free surface; **b** nondimensional time-averaged temperature, TNM , in sections A1, A and C. *Dotted lines* show approximate extent of the thermal MI close to the free surface. The *black circles* visualize the cores of the main SOV cells in the mean flow. MW denotes the mixing interface width at the free surface

on the CS side of the confluence is less than the temperature of the incoming CS flow. Still, the temperature field is far from approaching a uniform distribution on the CS side of the confluence.

The pattern of mean temperature distributions predicted by the model for Case 1 are consistent with temperature patterns documented in the field at KRCS [38, 52, 54]. Overall, DES successfully captures the evolution of the mean temperature field documented in the field for Case 1 by Rhoads and Sukhodolov [54] (Fig. 9). Both the DES results and the field data show that the MI, defined on the basis of a sharp lateral gradient in temperature, is narrow and close to vertical close to the junction apex (e.g., see section A3 in Fig. 9). Once SOV cells form and their circulation, Γ , is relatively high, the isotherms are distorted close



(a)



(b)

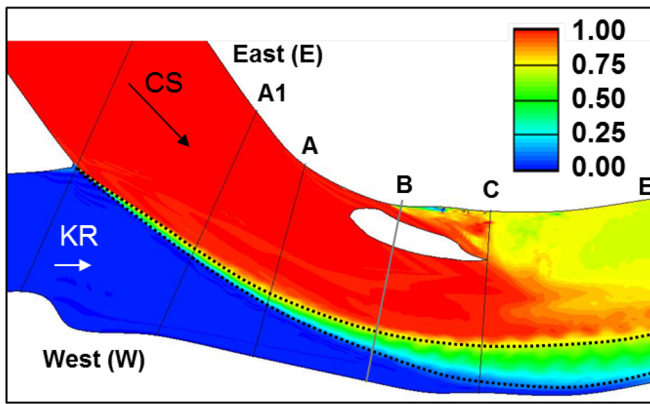
Fig. 11 Visualization of thermal mixing in the mean flow for Case 3. The nondimensional time-averaged temperatures of the incoming flow in streams KR and CS are $T_{NM} = 0$ and $T_{NM} = 1$, respectively. **a** Nondimensional time-averaged temperature, T_{NM} , in a horizontal surface situated $0.1 D$ below the free surface; **b** nondimensional time-averaged temperature, T_{NM} , in sections A1, A and C. *Dotted lines* show approximate extent of the thermal MI close to the free surface. The *black circles* visualize the cores of the main SOV cells in the mean flow. MW denotes the mixing interface width at the free surface

to the channel bed. The model predicts comparable amounts of isotherms distortion on the KR and CS sides of the confluence at sections A1 and A, where the strengths of SVE1 and SVW1 are approximately equal. Distortion of the isotherms near the bed on the West side of the confluence is more pronounced in the simulation than in the field data, but both the simulation and field data show similar amounts of distortion on the East side of the confluence. Due to advection of near-bed fluid laterally by the SOV cells, the spacing between the isotherms increases in the near-bed region. Once the circulation of SVE1 is much larger than that of SVW1 (e.g., the difference is close to 40 % at section C), the isotherms exhibit strong deformation near the bed on the East side of the confluence, becoming nearly horizontal in alignment and spread widely apart. Meanwhile, the isotherms remain close to vertical on the West side of the confluence. This transformation of the isotherms in the field data is well captured by DES (e.g., Fig. 9a, section C). The simulation model adds strong support to the claim that this characteristic distortion of mean temperature isotherms at KRCS is the result of strong vertical motion of the flow inward over the CS side of the downstream channel as flow in the CS curves to become aligned with the orientation of this channel [38, 52, 54]. Thus, helical motion plays a prominent role in mixing of confluent flows at KRCS.

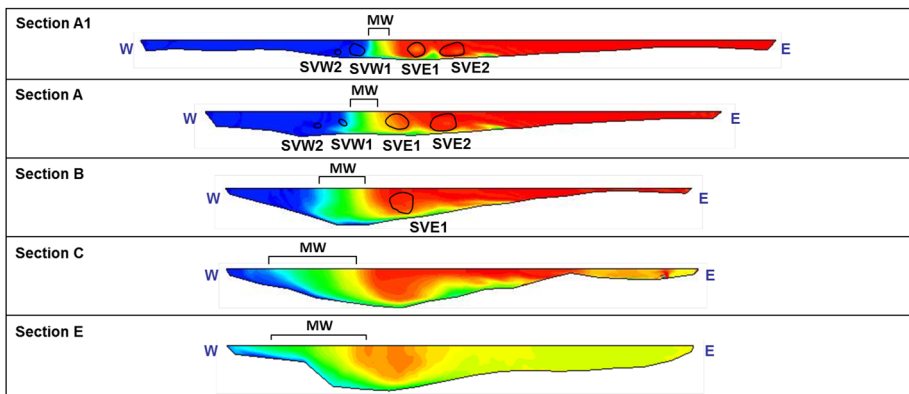
As opposed to Case 1 where the thermal MI in the mean flow is nearly vertical (Fig. 8), in Case 2 the boundaries of the MI are strongly tilted in the vicinity of the upstream junction corner (Fig. 10). The tilt is toward the West bank near the free surface. The core of high-momentum, warmer, fluid from the CS stream approaches the MI at a relatively high angle and pushes the thermal MI toward the West bank. Meanwhile, the core of high momentum fluid in the incoming KR stream is oriented toward the West bank and thus cannot compensate for the effect of the high-momentum fluid in the CS on the MI, even though $Mr \approx 1$. Due to bottom friction and the relative position of the core of high velocity magnitude in the incoming CS stream, the lateral displacement of the MI is larger close to the free surface compared to the near-bed region. As a result, a near-bed intrusion containing unmixed colder fluid underlies the MI on the KR side of the confluence. Downstream of section A, strong vertical motion on the CS side of the channel (SVE1 and SVE2) enhances the near-bed penetration of this mass of cool water toward the East bank, beneath the overlying CS flow. Thus, the effect of helical motion on mixing documented in Case 1 is enhanced in Case 2. The presence of the SOV cells, as well as the shear layer along the inner bank induced by the sharp change in the orientation of the bankline produce strong mixing on the CS side of the confluence. Given that advective effects associated with vertical motion are weak on the KR side of the MI and that turbulence generated at the West bank does not extend far into the flow, mixing on the KR side is weak even in the downstream part of the confluence hydrodynamic zone.

In Case 3, the width of the MI near the surface increases progressively over distance (Fig. 11a). Similar to Case 1, the MI is nearly vertical close to the free surface, at least over the upstream part of the confluence hydrodynamic zone (Fig. 11b). Then, the width of the thermal MI increases pretty suddenly. The reason for this increase is not an increase in the size of the quasi-2D MI eddies but rather the fact that the near-bed intrusion driven by the main SOV cell on the East side of the MI reaches the free surface a short distance downstream of section A (Fig. 11b). The coherent SOV cell on the KR side of the confluence (SVW1) (Fig. 2c) has no effect on mixing as this cell is displaced away from the MI (Fig. 11b). The main cell on the CS side of the confluence (SVE1), despite being less coherent and extending over a shorter distance in the streamwise direction than SVW1, plays a substantial role in mixing, at least close to the MI (Fig. 11b). Similar to the other cases where a SOV cell is situated in the vicinity of the

MI, this cell advects fluid laterally toward the East bank near the bed, leading to the development of a near-bed intrusion of cool water on the CS side of the MI. Fluid entrained by SVE1 is transported inward and upward toward the free surface near the MI as the cell enlarges, but decreases in circulation strength (sections A1 to C, Fig. 11b). The absence of secondary SOV cells and the relatively weak circulation of SVE1 limit the lateral extent of advective mixing on the East side of the downstream channel. Most of the fluid from the intrusion containing fluid with a temperature close to the mean of the temperatures of the two incoming streams is injected into the core of SVE1. As one moves downstream, the core loses its circulation but increases its size such that, downstream of section A, the core of SVE1 reaches the free surface. Once this happens, it is impossible to distinguish between the average-temperature fluid within the MI and the one contained within the core of SVE1.



(a)



(b)

Fig. 12 Visualization of thermal mixing in the mean flow for Case 4. The nondimensional time-averaged temperatures of the incoming flow in streams KR and CS are $TNM = 0$ and $TNM = 1$, respectively. **a** nondimensional time-averaged temperature, TNM , in a horizontal surface situated $0.1 D$ below the free surface; **b** nondimensional time-averaged temperature, TNM , in sections A1, A, B, C and E. *Dotted lines* show approximate extent of the thermal MI close to the free surface. The *black circles* visualize the cores of the main SOV cells in the mean flow. MW denotes the mixing interface width at the free surface

The mean temperature distribution in Case 4 differs from distributions for the other 3 cases. The strong KH mode induces vortex pairing which results in streamwise growth of the quasi-2D MI eddies, thereby producing a high rate of increase in the width of the MI (Fig. 12a). The position of the MI toward the outer bank is influenced both by the high momentum ratio of the incoming flow and by topographic forcing of the flow outward by the submerged bar on the East side of the downstream channel. The relatively strong SOV cells on the CS of the MI (Fig. 2d) lead to pronounced near-bed intrusions of cool water on this side of the confluence as fluid from the MI is entrained into the cells. This advective mixing is reflected by increases in the spacing between the isotherms away from the centerline of the MI, especially near bed (Fig. 12b). Inward and upward motion of the flow induced by vortical motion transports cool water over the entire inner portion of the downstream channel. The simulation results here provide strong support for this argument. Downstream of section C, the MI eddies start interacting with the West bank and thermal mixing increases rapidly on the KR side of the confluence. At section E, the mean temperature distribution is close to uniform over most of the CS side of the confluence. Only in the immediate vicinity of the MI is a core of warmer fluid from the incoming CS flow still visible. This pattern of thermal mixing, in which cool water from the KR is advected inward and upward by strong helical motion producing an isolated remnant of warm fluid over the thalweg, has been extensively documented at KRCS and has been attributed to the advective action of helical motion over the inner portion of the downstream channel [38]. The results here provide numerical corroboration of the mechanism driving this pattern of mixing.

6 Conclusions

Numerical simulations of flow and temperature transport conducted with a model that can resolve the unsteady dynamics of large-scale turbulence and coherent structures in the mean flow were used to investigate the main mechanisms of thermal mixing at a small stream confluence under various inflow conditions (e.g., momentum flux ratio of the incoming streams) and planform geometries (e.g., angles between the incoming streams and angles between the incoming streams and the downstream channel). Coupled with previous validation of the numerical predictions of the mean velocity and TKE fields based on conditions at the Kaskaskia River-Copper Slough confluence [16, 18, 20], the results presented here show that the numerical model of confluence hydrodynamics can be used to understand the physics of thermal mixing at confluences, and, in particular, the role played by the large-scale coherent structures in mixing processes. Results for the case corresponding to bathymetric and flow conditions measured by Rhoads and Sukhodolov [54] at the confluence of the Kaskaskia River (KR) and Copper Slough (CS) show that patterns of thermal mixing in the simulation are similar to those documented in the field. In particular, the model reproduces the distortion of the mixing interface through tilting and the penetration of cool water from the main stem (KR) beneath warm water from the lateral tributary (CS) through advective transport induced by vortical motion within the tributary flow. This vortical motion develops as the flow from the lateral tributary curves to become aligned with the orientation of the downstream channel. Thus, the simulation results provide additional support and clarification for the argument based on analysis of patterns of temperature and flow [38] that thermal mixing at the Kaskaskia River-Copper Slough confluence is strongly influenced by vortical motion on the Copper Slough side of the

mixing interface. This vortical motion, through interaction with large-scale turbulent structures within the MI, entrains cool fluid from the Kaskaskia River and transports it inward and upward over the Copper Slough side of the downstream channel.

The strong advective effects of SOV cells on mixing indicate that evaluations of thermal mixing between the two streams based only on free surface data may be misleading as the surface may not reflect subsurface processes. Access to 3D temperature data is essential to understand thermal mixing, especially for confluences where strongly-coherent SOV cells form or where bathymetry has a strong effect on mixing, such as discordant confluences [6]. For all the cases where SOV cells form in the vicinity of the MI, treating the flow as a quasi-2D flow or using simplified analytical models based on the depth-averaged equations will result in gross prediction errors for the mean temperature distribution inside the confluence hydrodynamic zone.

The results also support the argument that this pattern of mixing is driven mainly by inertial effects associated with vortical motion of the flow, rather than by buoyancy effects associated with thermal differences between the confluent flows, which are neglected in the model and which do not exhibit a strong relationship with mixing in empirical analysis of field data [38]. Recent work indicates that buoyancy effects can have substantial effects on mixing under certain conditions [1, 5, 40, 46] and further work is needed to examine this issue in detail, including incorporation of such effects in numerical simulations.

More generally, analysis of the instantaneous and mean vorticity and temperature flow fields for the four test cases considered in the present study have clearly confirmed the important role that SOV cells play in thermal mixing at confluences of different configurations and incoming flow conditions. The capacity of the SOV cells to promote thermal mixing is the largest when the cores of these cells are situated close to the MI and where the cores of adjacent co-rotating cells are subject to large-scale bimodal motions toward and away from the MI. A large angle between one or both of the tributaries and the downstream channel, which leads to substantial curvature of flow streamlines, favors the development of strong SOVs and thus thermal mixing through lateral advection of fluid within the confluence hydrodynamic zone. A SOV can develop even when the upstream channels are aligned with the downstream channel; however, under such conditions the spatial extent of the cell is limited, as is the influence of the cell on lateral mixing.

The numerical simulations demonstrate how mechanisms that generate and promote the downstream growth of the quasi-2D MI eddies within the MI influence mixing by producing interpenetration of confluent flows. Mixing by interpenetration is strongest for MIs where the KH mode is well-developed at and downstream from the upstream junction corner. Under these conditions the width of the MI increases downstream as a result of vortex pairing. Large-scale eddies can also generate substantial interpenetration of the two flows for cases when the wake mode is strong. Under these conditions, interactions between shear layers bounding a well-developed zone of stagnant fluid at the upstream junction corner generate highly-coherent eddies within the MI in the form of a vortex street.

Thermal mixing is enhanced the most when a large junction angle and momentum flux ratio promote the development of strong SOVs within the portion of the flow originating from the lateral tributary as well as the development of large KH eddies that pair in the downstream direction within the MI (Case 4 in the present study). Under these conditions the two streams fully mix a short distance downstream of the confluence hydrodynamic zone. The least amount of thermal mixing within the confluence hydrodynamic zone occurs when both incoming streams are nearly parallel with the downstream channel and mixing is confined to a small region close to the MI (Case 3 in the present study). For this case,

both the wake mode and the KH mode remain relatively weak along the MI. So, both main mechanisms promoting large-scale thermal mixing are weak.

The differences in the spatial development, position and size of the region containing fluid with temperatures between those of the two incoming streams in the four test cases illustrate the difficulties in generalizing the process of mixing of flows at confluences, even for cases that do not consider density effects or the influence of bed discordance on mixing. This study examined mixing at small stream confluences and scale is another issue that deserves consideration [51]. Large-scale secondary motion of the flow may not occur as commonly at confluences of large rivers as it does at small confluences and local factors, such as bathymetric effects, may play an important role in mixing at large river confluences. Density contrasts may also be more common where rivers draining substantially different source areas join [36]. Moreover, the increase in width-depth ratio of river channels within increasing channel size may limit the proportional effectiveness of coherent turbulent structures within the mixing interface to penetrate into adjacent flows [51], especially when frictional effects limit the downstream growth rates of these structures [12]. The lack of strong vortical motion, along with the restricted effectiveness of coherent structures on mixing in large, wide channels, may explain the lack of mixing observed over long distances downstream of confluences in many large river systems [7, 41, 47]. Unraveling the complexity of mixing at confluences is challenging, but, as this study has shown, numerical simulations provide a powerful tool for examining in detail how differences in boundary conditions affect process mechanisms.

Acknowledgments The authors would like to thank the Transportation Research and Analysis Computing Center (TRACC) at the Argonne National Laboratory and the National High-Performance Computing Center in Taiwan (NHPC) for providing substantial computing time. Part of this work was supported by the National Science Foundation under Grant GSS1359836. Any opinions, findings or recommendations expressed herein are those of the authors and do not necessarily reflect the views of the National Science Foundation

References

1. Arbat-Bofill M, Palau A, Sanchez-Junni M, Castellet EB, Ninerola D, Dolz J (2014) Hydrodynamics of Ribarroja reservoir (Ebro River, Spain): water temperature, water velocities and water age. In: Proceedings of the RiverFlow 2014 international conference on fluvial hydraulics, Lausanne, Switzerland, Ed. A. Schleiss, Taylor and Francis, London, UK
2. Ashmore PE, Ferguson RI, Prestegard KL, Ashworth PJ, Paola C (1992) Secondary flow in anabranch confluences of a braided, gravel-bed stream. *Earth Surf Process Landf* 17:299–311
3. Babarutsi S, Chu VH (1998) Modeling transverse mixing layer in shallow open-channel flows. *J Hydraul Eng* 124:718–727
4. Best JL (1988) Sediment transport and bed morphology at river channel confluences. *Sedimentology* 35:481–498
5. Biron PM, Lane SN (2008) Modelling hydraulics and sediment transport at river confluences. In: Rice SP, Roy AG, Rhoads B (eds) *River confluences, tributaries and the fluvial network*. Wiley, Chichester, pp 17–43
6. Biron PM, Ramamurthy A, Han S (2004) Three dimensional numerical modeling of mixing at river confluences. *J Hydraul Eng* 130:243–253
7. Bouchez J, Lajeunesse E, Gaillardet J, France Lanord C, Dutra Maia P, Maurice L (2010) Turbulent mixing in the Amazon River: the isotopic memory of confluences. *Earth Planet Sci Lett* 290:37–43
8. Bradbrook KF, Lane SN, Richards KS, Biron PM, Roy AG (2001) Role of bed discordance at asymmetrical river confluences. *J Hydraul Eng* 127:351–368
9. Bradbrook KF, Lane SN, Richards KS, Biron PM, Roy AG (2000) Large Eddy Simulation of periodic flow characteristics at river channel confluences. *J Hydraul Res* 38(3):207–215

10. Bradbrook KF, Lane SN, Richards KS (1998) Investigation of controls on secondary circulation in a simple confluence geometry using a three-dimensional model. *Hydrol Process* 12:1371–1396
11. Chang KS, Constantinescu G, Park SO (2007) Assessment of predictive capabilities of detached eddy simulation to simulate flow and mass transport past open cavities. *ASME J Fluids Eng* 129(11):1372–1383
12. Constantinescu G (2014) LE of shallow mixing interfaces: a review. *Environ Fluid Mech* 14:971–996. doi:[10.1007/s10652-013-9303-6](https://doi.org/10.1007/s10652-013-9303-6)
13. Constantinescu GS, Pasinato H, Wang YQ, Forsythe JR, Squires KD (2002) Numerical investigations of flow past a prolate spheroid. *J Fluids Eng ASME* 124(4):904–910
14. Constantinescu G, Chapelet MC, Squires KD (2003) Turbulence modeling applied to flow over a sphere. *AIAA J* 41(9):1733–1743
15. Constantinescu GS, Squires KD (2004) LES and DES investigations of turbulent flow over a sphere at $Re = 10,000$. *Flow Turbul Combust* 70:267–298
16. Constantinescu GS, Miyawaki S, Rhoads B, Sukhodolov A, Kirkil G (2011) Structure of turbulent flow at a river confluence with a momentum and velocity ratios close to 1: insight from an eddy-resolving numerical simulation. *Water Resour Res* 47:W05507. doi:[10.1029/2010WR010018](https://doi.org/10.1029/2010WR010018)
17. Constantinescu G, Koken M, Zeng J (2011) The structure of turbulent flow in an open channel bend of strong curvature with deformed bed: insight provided by an eddy resolving numerical simulation. *Water Resour Res* 47:W05515. doi:[10.1029/2010WR010114](https://doi.org/10.1029/2010WR010114)
18. Constantinescu G, Miyawaki S, Rhoads B, Sukhodolov A (2012) Numerical analysis of the effect of momentum ratio on the dynamics and sediment entrainment capacity of coherent flow structures at a stream confluence. *J Geophys Res Earth Surf* 117:F04028. doi:[10.1029/2012JF002452](https://doi.org/10.1029/2012JF002452)
19. Constantinescu G, Kashyap S, Tokyay T, Rennie CD, Townsend RD (2013) Hydrodynamics processes and sediment erosion mechanisms in an open channel bend of strong curvature with deformed bathymetry. *J Geophys Res Earth Surf* 118:480–496. doi:[10.1002/jgrf.20042](https://doi.org/10.1002/jgrf.20042)
20. Constantinescu G, Miyawaki S, Rhoads B, Sukhodolov A (2014) Numerical evaluation of the effects of planform geometry and inflow conditions on flow, turbulence structure, and bed shear velocity at a stream confluence with a concordant bed. *J Geophys Res Earth Surf* 119:2079–2097. doi:[10.1002/2014JF003244](https://doi.org/10.1002/2014JF003244)
21. Frias C, Abad JD (2013) Large eddy simulation (LES) for superimposed bedforms in fluvial channels. *Water Resour Res* 49:6548–6560. doi:[10.1002/wrcr.20456](https://doi.org/10.1002/wrcr.20456)
22. Gaudet JM, Roy AG (1995) Effect of bed morphology on flow mixing length at river confluences. *Nature* 373:138–139
23. Guneralp I, Abad JD, Zolezzi G, Hooke J (2012) Advances and challenges in meandering channels research. *Geomorphology* 163–164:1–9
24. Gutierrez R, Abad JD (2014) On the analysis of the medium term planform dynamics of meandering rivers. *Water Resour Res*. doi:[10.1002/2012WR013358](https://doi.org/10.1002/2012WR013358)
25. Hunt JCR, Wary AA, Moin P (1988) Eddies, stream, and convergence zones in turbulent flows. In: *Proceedings of the 1998 summer program. Center for Turbulence Research, Stanford, CA, 1988*, pp 193–208
26. Keylock CJ, Constantinescu G, Hardy RJ (2012) The application of computational fluid dynamics to natural river channels: eddy resolving versus mean flow approaches. *Geomorphology* 179:1–20. doi:[10.1016/j.geomorph.2012.09.006](https://doi.org/10.1016/j.geomorph.2012.09.006)
27. Kiffney PM, Greene C, Hall JE, Davies J (2006) Tributary streams create spatial discontinuities in habitat, biological productivity and diversity in mainstem rivers. *Can J Fish Aquat Sci* 63:2518–2530
28. Kirkil G, Constantinescu SG (2008) A numerical study of shallow mixing layers between parallel streams. In: *2nd international symposium on shallow flows, Hong Kong, December 2008*
29. Kirkil G, Constantinescu SG (2009) A numerical study of vertical non-uniformity of flow and mass exchange processes in a shallow turbulent mixing layer. In: *6th international symposium on turbulence, heat and mass transfer, Rome, Italy, September 2009*
30. Kirkil G, Constantinescu G, Ettema R (2009) DES investigation of turbulence and sediment transport at a circular pier with scour hole. *J Hydraul Eng* 135(11):888–901. doi:[10.1061/\(ASCE\)HY.1943-7900.0000101](https://doi.org/10.1061/(ASCE)HY.1943-7900.0000101)
31. Kirkil G, Constantinescu G (2015) Effects of cylinder Reynolds number on the turbulent horseshoe vortex system and near wake of a surface-mounted circular cylinder. *Phys Fluids* 27:075102. doi:[10.1063/1.4923063](https://doi.org/10.1063/1.4923063)
32. Knispel S, Castella E (2003) Disruption of a longitudinal pattern in environmental factors and benthic fauna by a glacial tributary. *Freshw Biol* 48:604–618

33. Koken M, Constantinescu G (2009) An investigation of the dynamics of coherent structures in a turbulent channel flow with a vertical sidewall obstruction. *Phys Fluids* 21:085104. doi:[10.1063/1.3207859](https://doi.org/10.1063/1.3207859)
34. Koken M, Constantinescu G, Blanckaert K (2013) Hydrodynamic processes, sediment erosion mechanisms, and Reynolds-number-induced scale effects in an open channel bend of strong curvature with flat bathymetry. *J Geophys Res Earth Surf* 118:2308–2324. doi:[10.1002/2013JF002760](https://doi.org/10.1002/2013JF002760)
35. Laizet S, Lardeau S, Lamballais E (2010) Direct numerical simulation of a mixing-layer downstream a thick splitter plate. *Phys Fluids* 22:015104
36. Laraque A, Guyot JL, Filizola N (2009) Mixing processes in the Amazon River at the confluences of the Negro and Solimões rivers, Encontro das Águas, Manaus, Brasil. *Hydrol Process* 23:3131–3140
37. Leite Ribeiro M, Blanckaert K, Roy AG, Schleiss AJ (2012) Flow and sediment dynamics in channel confluences. *J Geophys Res* 117:F01035. doi:[10.1029/2011JF002171](https://doi.org/10.1029/2011JF002171)
38. Lewis QW, Rhoads B (2015) Rates and patterns of thermal mixing at a small stream confluence under variable incoming flow conditions. *Hydrol Process*. doi:[10.1002/hyp10496](https://doi.org/10.1002/hyp10496)
39. Liou WW (1994) Linear instability of curved free shear layers. *Phys Fluids* 6(2):541–549
40. Lyubimova T, Lepikhin A, Kononov V, Parshakova Y, Tiunov A (2014) Formation of the density currents in the zone of confluence of two rivers. *J Hydrol* 508:328–342
41. Mackay JR (1970) Lateral mixing of the Liard and Mackenzie rivers downstream from their confluence. *Can J Earth Sci* 7(1):111–124
42. Marion A, Zaramella M (2006) Effects of velocity gradients and secondary flow on the dispersion of solutes in curved channels. *J Hydraul Eng ASCE* 132(12):1295–1302
43. Paola C (1997) When streams collide. *Nature* 387:232–233
44. Plesniak MW, Mehta RD, Johnson J (1996) Curved two-stream turbulent mixing layers revised. *Exp Thermal Fluid Sci* 13:190–205
45. Prats J, Armengol J, Marcé R, Sánchez-Juny M, Dolz J (2010) Dams and reservoirs in the lower Ebro River and its effects on the river thermal cycle, Hdb. *Environ Chem* 13:77–95
46. Ramon CL, Hoyer AB, Armengol J, Dolz J, Rueda FJ (2013) Mixing and circulation at the confluence of two rivers entering a meandering reservoir. *Water Resour Res* 49:1429–1445
47. Rathbun RE, Rostad CE (2004) Lateral mixing in the Mississippi River below the confluence with the Ohio River. *Water Resour Res* 40:W05207. doi:[10.1029/2003WR002381](https://doi.org/10.1029/2003WR002381)
48. Rice S (1998) Which tributaries disrupt downstream fining along gravel-bed rivers? *Geomorphology* 22:39–56
49. Rice SP, Kiffney P, Greene C, Pess GR (2008) The ecological importance of tributaries and confluences. In: Rice SP, Roy AG, Rhoads B (eds) *River confluences, tributaries and the fluvial network*. Wiley, Chichester, pp 17–32
50. Riley JD, Rhoads B, Parsons DR, Johnson KK (2015) Influence of junction angle on three-dimensional flow structure and bed morphology at confluent meander bends during different hydrological conditions. *Earth Surf Proc Land* 40:252–271
51. Rhoads BL (1996) Mean structure of transport-effective flows at an asymmetrical confluence when the main stream is dominant. In: Ashworth PJ, Best JL, Bennett SL, McLelland SJ (eds) *Coherent flow structures in open channels*. Wiley, New York, pp 491–517
52. Rhoads BL, Kenworthy ST (1995) Flow structure at an asymmetrical stream confluence. *Geomorphology* 11:273–293
53. Rhoads BL, Kenworthy ST (1998) Time averaged flow structure in the central region of a stream confluence. *Earth Surf Proc Land* 23:171–191
54. Rhoads BL, Sukhodolov AN (2001) Field investigation of three-dimensional flow structure at stream confluences: 1. Thermal mixing and time-averaged velocities. *Water Resour Res* 37(9):2393–2410
55. Rhoads BL, Sukhodolov AN (2004) Spatial and temporal structure of shear layer turbulence at a river confluence. *Water Resour Res* 40:W06304. doi:[10.1029/2003WR002811](https://doi.org/10.1029/2003WR002811)
56. Rhoads BL, Sukhodolov AN (2008) Lateral momentum flux and spatial evolution of flow within a confluence mixing interface. *Water Resour Res* 44:WR08440. doi:[10.1029/2007WR006634](https://doi.org/10.1029/2007WR006634)
57. Rodi W, Constantinescu G, Stoesser T (2013) Large eddy simulation in hydraulics IAHR Monograph. CRC Press, Taylor & Francis Group. ISBN-10: 1138000247
58. Sandham ND, Sandberg RD (2009) Direct numerical simulation of the early development of a turbulent mixing layer downstream of a splitter plate. *J Turbul* 10:1–17
59. Spalart PR, Allmaras SR (1994) A one-equation turbulence model for aerodynamic flows. *La Recherche Aérospatiale* 1:5–21
60. Spalart P (2009) Detached eddy simulation. *Annu Rev Fluid Mech* 41:181–202
61. Sukhodolov AN, Rhoads BL (2001) Field investigation of three-dimensional flow structure at stream confluences: 2. Turbulence. *Water Resour Res* 37:2411–2424

62. Winant CD, Browand FK (1974) Vortex pairing: the mechanism of turbulent mixing layer growth at moderate Reynolds numbers. *J Fluid Mech* 63:237–255
63. Wipfli M, Gregovich D (2002) Export of invertebrates and detritus from fishless headwater streams in southeastern Alaska: implications for downstream salmonid problem. *Freshw Biol* 47:957–970
64. Yalin MS, da Silva AMF (2001) *Fluvial processes*. Kluwer (IAHR) Monograph, Delft. ISBN 90-805649-2-3